

Parity switching in a full-shell superconductor-semiconductor nanowire qubit

O. Erlandsson,^{1,*} D. Sabonis,^{1,2,*} A. Kringhøj,¹ T.W. Larsen,¹ P. Krogstrup,¹ K. D. Petersson,¹ and C. M. Marcus¹

¹Center for Quantum Devices, Niels Bohr Institute, University of Copenhagen, 2100 Copenhagen, Denmark

²Laboratory for Solid State Physics, ETH Zürich, CH-8093 Zürich, Switzerland

(Dated: February 15, 2022)

The rate of charge-parity switching in a full-shell superconductor-semiconductor nanowire qubit is measured by directly monitoring the dispersive shift of a readout resonator. At zero magnetic field, the measured switching time scale T_P is on the order of 100 ms. Two-tone spectroscopy data post-selected on charge-parity is demonstrated. With increasing temperature or magnetic field, T_P is at first constant, then exponentially suppressed, consistent with a model that includes both non-equilibrium and thermally activated quasiparticles. As T_P is suppressed, qubit lifetime T_1 also decreases. The long $T_P \sim 0.1$ s at zero field is promising for future development of qubits based on hybrid nanowires.

The coherent manipulation of any transmon qubit is threatened by the presence of unpaired quasiparticles (QPs) in the superconductor, a problem referred to as quasiparticle poisoning (QPP). Understanding the nature and rate of QPP is therefore part of the challenge of using these superconducting circuits to construct complex quantum information processing devices. In a transmon qubit [1], a Josephson junction (JJ) with an associated energy E_J separates two superconductors which are shunted by a large capacitance with a charging energy E_C . As QPs tunnel across the JJ, they contribute to relaxation if they carry energy matching the qubit transition, and to dephasing in the case of non-vanishing charge dispersion.

Hybrid superconductor-semiconductor nanowire (NW) variants of the transmon qubit [2, 3] provide an alternative to conventional metallic systems. The semiconductor platform offers advantages such as control of E_J by electrostatic gating, and reduced charge dispersion without loss of anharmonicity [4, 5]. The system has been developed to be compatible with large magnetic fields [6–9] where it potentially could be used for topological quantum computation [10, 11]. With a magnetic field applied, NWs with a fully covering superconducting shell have been shown to exhibit destructive Little-Parks effect, both in dc transport and qubit measurements [12, 13].

In this Letter, the rate of QPP is measured in a full-shell superconductor-semiconductor hybrid NW qubit. It is found that QPP occurs on a timescale of $T_P \sim 0.1$ s, which is far from limiting the coherence time of the qubit. As either the temperature or magnetic field is increased, T_P is first constant then exponentially suppressed, suggesting the existence of both a non-equilibrium and equilibrium population of QPs in the qubit. Additionally, while the qubit frequency recovers in the first Little-Parks lobe, T_P remains below our detectable range (not sufficiently exceeding 30 μ s) after the initial suppression.

QPP in transmons was first measured directly by a Ramsey-type pulse sequences sensitive to the charge-parity state of the qubit [14]. This technique was subse-

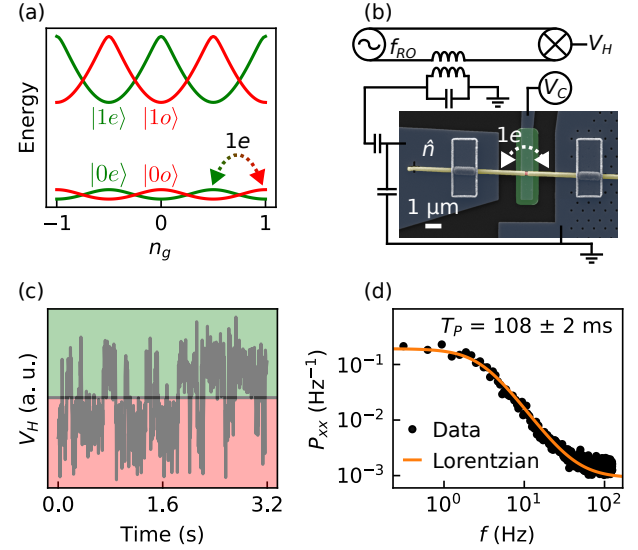


FIG. 1. (a) Parity branches of ground and excited states of the transmon Hamiltonian. The dotted arrow symbolizes a charge-parity switch (poisoning) as a quasiparticle tunnels across the Josephson junction. (b) False-color scanning electron micrograph of device and diagram of surrounding cQED circuit. An InAs (red) nanowire with an Al (yellow) shell is embedded in a NbN (blue; rectangular contacts to nanowire are NbTiN) structure on a Si substrate (black). A layer of HfO₂ (green) separates the bottom gate V_C from the etched junction. (c) Time trace of demodulated transmission V_H through the readout resonator, showing discrete switching, interpreted as changes of charge-parity state. Data taken at $T = 30$ mK and $B = 0$. The horizontal line between differently colored regions indicates data binning threshold. (d) Average power spectrum density of 40 traces fitted to a Lorentzian distribution, with T_P as given by the fit.

quently used to study transitions across all four parity-logical states [15] and the effect of shielding and qubit geometry on QPP levels [16, 17]. A technique based on direct dispersive monitoring of the charge-parity has also been developed [18]. This was recently used to study QPP in NWs similar to those investigated here but with the superconducting shell only covering half the facets,

where it was found that QPP occurred on the timescale of $100\text{ }\mu\text{s}$ and could have a non-monotonic dependence on magnetic field [9]. The effect of geometry was also studied with the dispersive technique [19]. Typical reported QPP time scales have ranged from $100\text{ }\mu\text{s}$ up to 1 s [9, 14–19]. Methods to mitigate unwanted quasiparticles in superconducting circuits have included qubit pumping [20] and trapping of quasiparticles by vortices [21, 22] or regions of normal metal [23].

QPP is measured as the rate of transitions between the two parity branches of the transmon. How QPP leads to dephasing (for non-vanishing charge dispersion) can be understood by considering the transmon Hamiltonian, $\hat{H} = 4E_C(\hat{n} - n_g)^2 - E_J \cos \hat{\phi}$, where n is the number of Cooper pairs on the island, n_g is the effective offset charge and ϕ is the phase difference across the JJ. As indicated in Fig. 1(a), each time a poisoning event occurs n_g is shifted by $1e$, which except for at degeneracy points, changes the qubit transition frequency, contributing to qubit dephasing and establishing two distinct charge-parity branches (even and odd) of each logical state. The charge-parity state is measured by monitoring the microwave transmission through the resonator, sensitive to changes in qubit transition frequency via the dispersive shift.

We now describe the experimental set-up to realize a transmon using a NW. To fabricate the sample, a 35 nm thick NbN film was sputtered onto a Si substrate. The cQED architecture, consisting of a microwave feedline, readout resonators, qubit islands, gate lines, and ground plane, was patterned in the NbN film by reactive ion etching. The cQED circuit is shown in Fig. 1(b). For the qubit studied here, the island was designed for a charging energy $E_C/h = 500\text{ MHz}$ and the resonator frequency $f_{\text{RO}} = 5.4\text{ GHz}$. The islands were connected to the ground plane by micromanipulator deposited VLS-grown InAs NWs with a full superconducting Al shell, placed on bottom gates covered by local HfO_2 dielectric. The Al shell had a small segment removed by wet etching, forming the semiconducting weak link of the JJ. Crossovers formed by crosslinked resist on HfO_2 tied the ground plane together across cQED features. NWs and crossovers were contacted to the NbN film by ion milling followed by sputtering of NbTiN. The sample was wire-bonded and placed in an In-sealed CuBe box filled with Eccosorb, which was loaded into a dilution refrigerator with a base temperature of $\sim 30\text{ mK}$. After passing through the sample, microwave signals were amplified by a traveling-wave parametric amplifier at base temperature and a cryogenic amplifier at 4 K . A 6-1-1 T vector magnet was used to apply a magnetic field in the plane of the substrate, along the axis of the NW.

Measurement of the charge-parity switching rate was first performed at base temperature and zero magnetic field. In order for the dispersive QPP signal to be visible, the qubit frequency f_{01} must be in the vicinity of

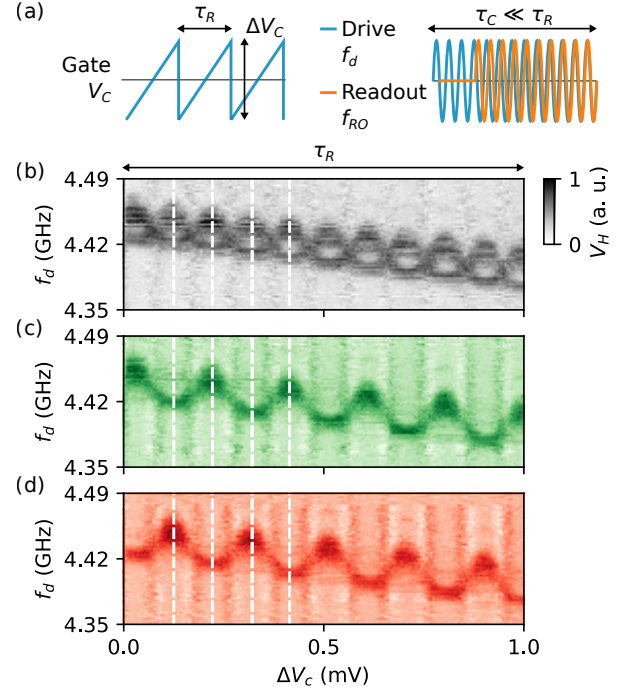


FIG. 2. Parity-resolved spectroscopy of transmon charge dispersion. (a) Gate voltage and microwave pulse scheme for measurement. V_C is ramped, while drive and readout tones are transmitted through the device. (b) All data averages, showing two peaks at each gate value (even and odd charge-parity branches). (c-d) Due to slow quasiparticle poisoning compared to the duration of the spectroscopy measurement, the data can be post-selected as into distinct parity branches. The small ΔV_C used here to control n_g also varies E_J , resulting in the overall slope of features in (b-d). Vertical white dashed lines are guides to the eye. Column averages are subtracted for enhanced visibility.

the readout resonator frequency $f_{\text{RO}} = 5.4\text{ GHz}$. Setting $V_C = -0.71\text{ V}$ gave $f_{01} = 4.1\text{ GHz}$, detected by two-tone spectroscopy. The transmission at the resonator frequency was monitored for 3.2 s , yielding time traces as shown in Fig. 1(c). The aggregated power spectral density P_{xx} of 40 binned time traces was fit using a Lorentzian form

$$S(f) = A \frac{T_P}{(\pi T_P f)^2 + 1} + B, \quad (1)$$

with poisoning time T_P , amplitude A and background B as fit parameters. Experimental data along with the resulting fit are shown in Fig. 1(d), yielding a low-temperature zero-field poisoning time of $T_P \sim 0.1\text{ s}$. This is on the higher end of values reported in similar systems.

Large T_P compared to the measurement duration means that the charge-parity branches of the qubit transition spectrum can be probed separately. In order to demonstrate this, the charge dispersion is probed and the data is post-selected according to charge parity. A ramped voltage is applied to the gate V_C and a two-

tone spectroscopy measurement is performed, as shown in Fig. 2(a). The ramped voltage was offset around -0.33 V, yielding $f_{01} \sim 4.4$ GHz. Around this offset, a small ramp amplitude ΔV_C was used to control the effective charge-offset n_g . Typically, this results in the pattern in Fig. 2(b) where both charge-parity branches are visible [24]. However, because the ramp signal and data acquisition can be applied considerably faster than QPP, the two charge-parity branches can be separated by post-selection [25], as shown in Figs. 2(c,d). A different technique for parity-selective spectroscopy based on interspersed parity measurements was recently demonstrated for Andreev bound states [26].

Temperature dependence of QPP is shown in Fig. 3. Below 80 mK, QPP time T_P was found to be independent of temperature T . Above 80 mK, T_P is exponentially suppressed. Assuming a QP density x_{QP} with a fixed contribution x_{QP}^0 from non-equilibrium QPs as well as a thermally activated contribution, the total QP density, normalized by the Cooper pair density, is given by [27],

$$x_{QP} = x_{QP}^0 + \sqrt{2\pi k_B T / \omega} \exp(-\omega / k_B T) \quad (2)$$

where ω is the superconducting spectral gap. Assuming that $1/T_P = C x_{QP}$ where C is an unknown proportionality constant, and fitting to the logarithm of data points yields the fit in Fig. 3(a). The resulting $\omega = (139 \pm 2) \mu\text{eV}$ is in reasonable agreement with the bulk superconducting gap of Al $\sim 200 \mu\text{eV}$. The density of non-equilibrium QPs $x_{QP}^0 \sim 10^{-8}$ is among the lower values reported for similar systems [9, 15, 19].

Next, we investigate qubit coherence and QPP as a function of axial magnetic field B relevant for potential applications in topological quantum computation. The full-shell NW exhibits destructive Little-Parks effect [13] which is reflected in the reentrant structure of qubit frequency as a function of B [25]. We note, however, that the QP spectral gap ω is different from the pairing energy Δ , the latter determining the qubit frequency via $E_J = (\Delta/4) \sum \eta$, where η are the channel transmissions. Away from zero magnetic field, ω and Δ are distinct, as discussed in Sec. 10.2.2 of Ref. [28]. At each value of B , two-tone spectroscopy was performed and a simple peak-finding algorithm was used to identify the qubit frequency. Rabi and relaxation pulse sequences were then run at the qubit frequency. An exponential fit to the relaxation-sequence data gave T_1 , shown in Fig. 4.

The f_{01} data in Fig. 4(a) were fit using $f_{01} = f_0 \sqrt{\Delta(B)/\Delta(B=0)}$, where $\Delta(B)$ is governed by the destructive Little-Parks effect due to the full cylindrical superconducting shell of the NW [13, 25]. The fit yields an NW radius $R = 90$ nm, Al shell thickness $t = 4$ nm and superconducting coherence length $\xi = 165$ nm. The physical dimensions are in rough agreement with transmission electron micrographs of NWs from the same growth batch [25], although t is

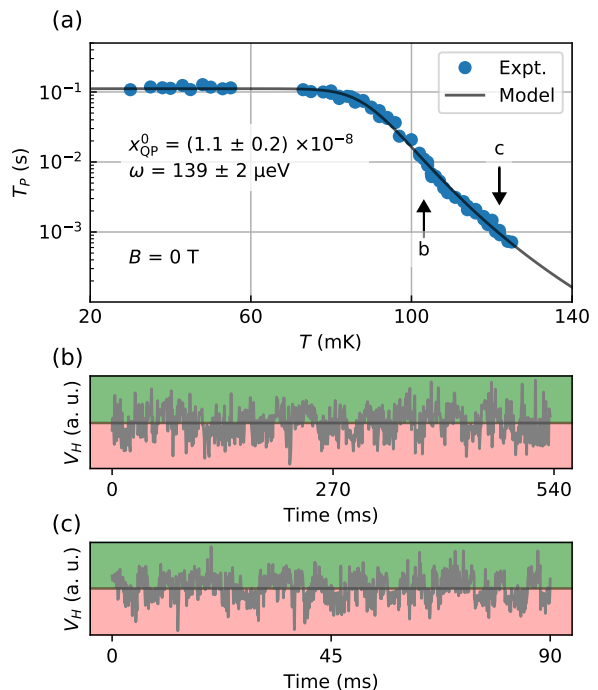


FIG. 3. Poisoning time T_P as a function of temperature T . (a) As T is increased, T_P is constant then starts to decrease exponentially around 80 mK. This is interpreted as the onset of significant contribution to QPP from thermally activated QPs. Model (black curve) yields good description of experimental data. (b, c) Examples of individual V_H time traces at different orders of magnitude of T_P , as indicated by the arrows in (a).

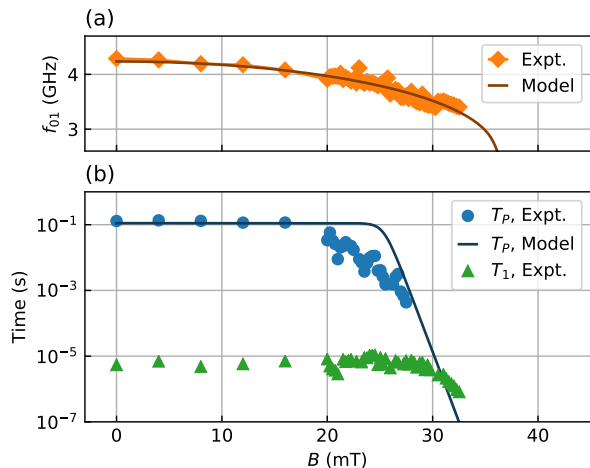


FIG. 4. Qubit frequency f_{01} , poisoning time T_P , and qubit relaxation time T_1 as functions of magnetic field B along the NW axis. (a) f_{01} is suppressed as a function of B . The data are fit to $\Delta(B)$ as described by the Little-Parks effect (black curve). (b) T_P is first constant, then diminishes above 20 mT. As T_P is further suppressed, T_1 starts to reduce, suggesting that T_1 becomes limited by QPP.

considerably small. In Fig. 4(b), measured T_P , T_1 are plotted along with a model for T_P as calculated by (2) using the parameters from the f_{01} fit, and C , $\omega(B=0)$, x_{QP}^0 from the fit to temperature-dependent data in Fig. 3(a) and $T=30$ mK (base temperature). Here $\omega(B)$ is also governed by the Little-Parks effect [25]. The onset of increasing QPP occurs at a lower magnetic field than predicted by the model. The reason for this discrepancy may be related to changes in the quasiparticle density of states at finite field, where it is no longer exponential as assumed in (2). The NW gap is softened at finite field [29] and the coherence peaks are broadened [28]. Furthermore, the magnetic-field dependence of the non-equilibrium QP population is unknown.

Although QPP imposes a limit on qubit coherence, the ground state switching measured in this work ($|0e\rangle \leftrightarrow |0o\rangle$) does not itself relax the qubit, since it is a transition between different charge-parities of the qubit ground state. However, the rate of QP-induced transitions that contribute to relaxation ($|0e\rangle \leftrightarrow |1o\rangle$ and $|0o\rangle \leftrightarrow |1e\rangle$) are also related to the QP density, and the similar magnetic fields at which T_P and T_1 start to decrease in Fig. 4(b) suggests that QPP becomes the limiting factor on the qubit lifetime above 30 mT. The full-shell NW exhibits the Little-Parks effect, causing Δ and ω to revive as the field is further increased, with a first reentrant lobe centered around 100 mT [25]. At 100 mT, ω is predicted to have sufficiently recovered such that T_P is again dominated by non-equilibrium QPs. At this magnetic field, we measured $T_1 = 0.4 \mu\text{s}$, however, no split populations was observed in the dispersive charge-parity monitoring with $f_{01} = 3.5$ GHz, which we interpret as T_P not sufficiently exceeding the measurement integration time $\tau_I = 30 \mu\text{s}$. A likely cause of the enhanced QPP in the first lobe is the increased density of subgap states in that regime, as previously observed in the same NWs [30], increasing the QP density of states.

In conclusion, we have examined the rate of charge-parity switching in a full-shell superconducting-semiconducting nanowire qubit. We found a long parity switching time $T_P \sim 0.1$ s at zero field, and exponential suppression of T_P with field and temperature, in good qualitative agreement with our model. We interpret the exponential onset as associated with thermally activated QPs. Above 20 mT, this is observed as the rate of QPP rapidly increasing, coinciding with the collapse of the gap in the zeroth lobe of the Little-Parks effect. In the first lobe of reentrant superconductivity, T_P does not recover along with Δ , consistent with previously observed subgap states in this regime. The large value of T_P at zero magnetic field indicates that QPP is not a near-term barrier for the engineering of increased coherence times in this type of qubit.

METHODS

Data in Figs. 1 c-d: A total of $N_T = 40$ time traces of the in-phase and quadrature components of transmission response are recorded by heterodyne demodulation. Each trace consists of $N_P = 800$ points separated by $\tau_C = 4$ ms and integrated over $\tau_I = 100 \mu\text{s}$. For improved signal-to-noise ratio, the data are then projected onto a rotation angle in the phase-quadrature-plane, selected by eye, yielding a scalar V_H [25]. A single time trace is shown in Fig. 1(c). Following the analysis in Ref. [14], the data are binned such that points above (below) the mean value are assigned to 1 (−1). The binned data are then fit to the Lorentzian form in Eq. (2).

Data in Figs. 2 c-d: To control n_g , a ramp signal is applied to V_C with a period 2 ms, amplitude $\Delta V_C = 1$ mV and offset -0.33 V. This value of V_C is sufficiently small so that the gate mainly controls n_g and has a small effect on E_J (visible as the overall slope of features in Fig. 2). This is shown in Fig. 2(a), along with a variable qubit drive tone f_d and a readout tone at $f_{RO} = 5.4$ GHz. For each value of f_d , V_H is measured for 15 consecutive ramps, with 200 data points separated by $\tau_C = 10 \mu\text{s}$ taken per ramp period. These 15 ramp periods are averaged into one trace, plotted horizontally in Fig. 2(b-d). Accordingly, one trace takes $15 \times 200 \times \tau_C = 30$ ms to acquire. The drive tone f_d is stepped through a window of frequencies, and the entire process is then repeated 20 times. In Fig. 2(b), all 20 traces are averaged for each f_d , yielding a pearl-shaped pattern corresponding to the qubit charge dispersion.

Data in Fig. 3: For T_P to be probed over multiple orders of magnitude, it was not possible to acquire all data at fixed N_T and τ_C . This is because small τ_C is required to resolve small T_P , but such a sampling rate could not be sustained for the duration needed to capture $T_P \gg \tau_C$ due to memory limitations in data acquisition. Therefore, we repeated the temperature sweep trying different combinations of N_T , τ_C and τ_I at different T until we could measure T_P over a wide range of T . Furthermore, for simplicity, only integration times $\tau_I > T_1$ are used, in order to predominantly detect the ground states. Due to residual excited state population, all four states in Fig. 1(a) would be resolved for lower τ_I , and the transition rates would need distinguishing. For $\tau_I > T_1$, the visibility of the ground states dominates, and the analysis is straightforward. At base temperature and $B = 0$, $T_1 \sim 5 \mu\text{s}$ so we set $\tau_I > 20 \mu\text{s}$ for all data in Fig. 3 and Fig. 4. This simplification defines the lower bound of detectable T_P in those measurements ($T_P \gg 20 \mu\text{s}$).

Data in Fig. 4: Measurements of T_P are interleaved with measurements of f_{01} and T_1 . To achieve this, a measurement sequence was set up as follows. At each setpoint of B , two-tone spectroscopy was performed from which the qubit frequency was determined by a peak-finding

routine. At this frequency, standard Rabi and relaxation pulse schemes were used to determine the π pulse duration and T_1 , respectively. Finally, a measurement of T_P was performed; as for the data in Fig. 3, different combinations of N_T , τ_C and τ_I were used to resolve switching events at different B . At 104 mT, where no split population was observed, the measurement was performed using $N_T = 5$, $N_P = 2000$, $\tau_C = 100 \mu\text{s}$ and $\tau_I = 30 \mu\text{s}$.

ACKNOWLEDGMENTS

We thank Arno Bargerbos, Gijs de Lange, Leonid Glazman, Torsten Karzig, Dmitry Pikulin, Willemijn Uilhoorn, and Bernard van Heck for useful discussions. We thank Will Oliver for providing the traveling-wave parametric amplifier used in the experiment. We thank Martin Espiñeira for electron microscopy. We thank Marina Hesselberg, Karthik Jambunathan, Robert McNeil, Karolis Parfeniukas, Agnieszka Telecka, Shivendra Upadhyay, and Sachin Yadav at QDev, and Mahesh Kumar, Rizwan Ali, Tommi Riekkinen, and Pasi Kostamo at Espoo for device nanofabrication. Research is supported by the Danish National Research Foundation, Microsoft, European Research Commission grant 716655, and a grant (Project 43951) from VILLUM FONDEN.

* These authors contributed equally to this work

- [1] J. Koch, T. M. Yu, J. Gambetta, A. A. Houck, D. I. Schuster, J. Majer, A. Blais, M. H. Devoret, S. M. Girvin, and R. J. Schoelkopf, *Phys. Rev. A* **76**, 042319 (2007).
- [2] G. de Lange, B. van Heck, A. Bruno, D. J. van Woerkom, A. Geresdi, S. R. Plissard, E. P. A. M. Bakkers, A. R. Akhmerov, and L. DiCarlo, *Phys. Rev. Lett.* **115**, 127002 (2015).
- [3] T. W. Larsen, K. D. Petersson, F. Kuemmeth, T. S. Jespersen, P. Krogstrup, J. Nygård, and C. M. Marcus, *Phys. Rev. Lett.* **115**, 127001 (2015).
- [4] A. Bargerbos, W. Uilhoorn, C.-K. Yang, P. Krogstrup, L. P. Kouwenhoven, G. de Lange, B. van Heck, and A. Kou, *Phys. Rev. Lett.* **124**, 246802 (2020).
- [5] A. Kringhøj, B. van Heck, T. W. Larsen, O. Erlandsson, D. Sabonis, P. Krogstrup, L. Casparis, K. D. Petersson, and C. M. Marcus, *Phys. Rev. Lett.* **124**, 246803 (2020).
- [6] F. Luthi, T. Stavenga, O. W. Enzing, A. Bruno, C. Dickel, N. K. Langford, M. A. Rol, T. S. Jespersen, J. Nygård, P. Krogstrup, and L. DiCarlo, *Phys. Rev. Lett.* **120**, 100502 (2018).
- [7] J. Kroll, F. Borsoi, K. van der Enden, W. Uilhoorn, D. de Jong, M. Quintero-Pérez, D. van Woerkom, A. Bruno, S. Plissard, D. Car, E. Bakkers, M. Cassidy, and L. Kouwenhoven, *Phys. Rev. Applied* **11**, 064053 (2019).
- [8] A. Kringhøj, T. W. Larsen, O. Erlandsson, W. Uilhoorn, J. G. Kroll, M. Hesselberg, R. P. G. McNeil, P. Krogstrup, L. Casparis, C. M. Marcus, and K. D. Petersson, *Phys. Rev. Applied* **15**, 054001 (2021).
- [9] W. Uilhoorn, J. G. Kroll, A. Bargerbos, S. D. Nabi, C.-K. Yang, P. Krogstrup, L. P. Kouwenhoven, A. Kou, and G. de Lange, *arXiv:2105.11038* (2021).
- [10] E. Ginossar and E. Grosfeld, *Nature communications* **5**, 4772 (2014).
- [11] S. Vaitiekėnas, G. Winkler, B. van Heck, T. Karzig, M.-T. Deng, K. Flensberg, L. Glazman, C. Nayak, P. Krogstrup, R. Lutchyn, *et al.*, *Science* **367**, eaav3392 (2020).
- [12] S. Vaitiekėnas, P. Krogstrup, and C. M. Marcus, *Phys. Rev. B* **101**, 060507 (2020).
- [13] D. Sabonis, O. Erlandsson, A. Kringhøj, B. van Heck, T. W. Larsen, I. Petkovic, P. Krogstrup, K. D. Petersson, and C. M. Marcus, *Phys. Rev. Lett.* **125**, 156804 (2020).
- [14] D. Ristè, C. C. Bultink, M. J. Tiggelman, R. N. Schouten, K. W. Lehnert, and L. DiCarlo, *Nature Communications* **4**, 1913 (2013).
- [15] K. Serniak, M. Hays, G. de Lange, S. Diamond, S. Shankar, L. D. Burkhardt, L. Frunzio, M. Houzet, and M. H. Devoret, *Phys. Rev. Lett.* **121**, 157701 (2018).
- [16] C. Kurter, C. Murray, R. Gordon, B. Wymore, M. Sandberg, R. Shelby, A. Eddins, V. Adiga, A. Finck, E. Rivera, *et al.*, *arXiv preprint arXiv:2106.11488* (2021).
- [17] R. Gordon, C. Murray, C. Kurter, M. Sandberg, S. Hall, K. Balakrishnan, R. Shelby, B. Wacaser, A. Stabile, J. Sleight, *et al.*, *arXiv preprint arXiv:2105.14003* (2021).
- [18] K. Serniak, S. Diamond, M. Hays, V. Fatemi, S. Shankar, L. Frunzio, R. Schoelkopf, and M. Devoret, *Phys. Rev. Applied* **12**, 014052 (2019).
- [19] X. Pan, H. Yuan, Y. Zhou, L. Zhang, J. Li, S. Liu, Z. H. Jiang, G. Catelani, L. Hu, and F. Yan, *arXiv preprint arXiv:2202.01435* (2022).
- [20] S. Gustavsson, F. Yan, G. Catelani, J. Bylander, A. Kamal, J. Birenbaum, D. Hover, D. Rosenberg, G. Samach, A. P. Sears, S. J. Weber, J. L. Yoder, J. Clarke, A. J. Kerman, F. Yoshihara, Y. Nakamura, T. P. Orlando, and W. D. Oliver, *Science* **354**, 1573 (2016).
- [21] U. Vool, I. M. Pop, K. Sliwa, B. Abdo, C. Wang, T. Brecht, Y. Y. Gao, S. Shankar, M. Hatridge, G. Catelani, M. Mirrahimi, L. Frunzio, R. J. Schoelkopf, L. I. Glazman, and M. H. Devoret, *Phys. Rev. Lett.* **113**, 247001 (2014).
- [22] C. Wang, Y. Y. Gao, I. M. Pop, U. Vool, C. Axline, T. Brecht, R. W. Heeres, L. Frunzio, M. H. Devoret, G. Catelani, L. I. Glazman, and R. J. Schoelkopf, *Nature Communications* **5**, 5836 (2014).
- [23] U. Patel, I. V. Pechenezhskiy, B. L. T. Plourde, M. G. Vavilov, and R. McDermott, *Phys. Rev. B* **96**, 220501 (2017).
- [24] J. A. Schreier, A. A. Houck, J. Koch, D. I. Schuster, B. R. Johnson, J. M. Chow, J. M. Gambetta, J. Majer, L. Frunzio, M. H. Devoret, S. M. Girvin, and R. J. Schoelkopf, *Phys. Rev. B* **77**, 180502 (2008).
- [25] See Supplementary Material for details on data rotation in the phase-quadrature-plane, parity data post-selection, destructive Little-Parks effect, nanowire micrographs, and the experimental setup.
- [26] J. Wesdorp, L. Grünhaupt, A. Vaartjes, M. Pita-Vidal, A. Bargerbos, L. Splitthoff, P. Krogstrup, B. van Heck, and G. de Lange, *arXiv preprint arXiv:2112.01936* (2021).
- [27] G. Catelani, R. J. Schoelkopf, M. H. Devoret, and L. I. Glazman, *Phys. Rev. B* **84**, 064517 (2011).

- [28] M. Tinkham, *Introduction to Superconductivity*, 2nd ed., International Series in Pure and Applied Physics (McGraw Hill, New York, 1996).
- [29] W. Chang, S. M. Albrecht, T. S. Jespersen, F. Kuemmeth, P. Krogstrup, J. Nygård, and C. M. Marcus, *Nature Nanotechnology* **10**, 232 (2015).
- [30] A. Kringhøj, G. W. Winkler, T. W. Larsen, D. Sabonis, O. Erlandsson, P. Krogstrup, B. van Heck, K. D. Petersson, and C. M. Marcus, *Phys. Rev. Lett.* **126**, 047701 (2021).
- [31] I. Sternfeld, E. Levy, M. Eshkol, A. Tsukernik, M. Karpovski, H. Shtrikman, A. Kretinin, and A. Palevski, *Phys. Rev. Lett.* **107**, 037001 (2011).
- [32] V. H. Dao and L. F. Chibotaru, *Phys. Rev. B* **79**, 134524 (2009).
- [33] A. I. Larkin, *JETP* **21**, 153 (1965).

SUPPLEMENTARY MATERIAL

Rotation of data in phase-quadrature-plane

Here we describe the procedure for determining a rotation angle θ in the phase-quadrature-plane. For each measurement of T_P in the main text, a series of plots were generated for several different θ , as shown in Fig. S1 for the data set in Fig. 1(c-d) of the main text. The value of θ was selected to emphasize the bimodality of the two charge-parity populations, as visually apparent from histograms and time traces. Due to instability of n_g over time, the separation of the charge-parity population varies. Data sets where two main populations were not observed were not used to obtain values of T_P ; this situation could result e.g. from n_g on a degeneracy point, or a charge jump during the course of the measurement. For many data sets, phase-quadrature-plane histogram contained tail-like features, interpreted as partially resolved residual excited state population. In these cases, θ and angle was selected in a compromise between the axis connecting the charge-parity populations and the line orthogonal to the one connecting the residual features. In general, this is not the same as the line along the midpoints of the two populations. In the case of Fig. S1, this meant that $\theta = 1.369$ rad was selected (bottom row of plots). The particular criterion used in the selection of θ is not expected to introduce a bias in T_P , as the rotation does not directly alter time domain aspects of the data. For example, in the case of the data in Fig. 1(c-d) of the main text, the standard deviation of T_P values resulting from the Lorentzian fit, across a 1 rad interval around the selected angle, was found to be $< 5\%$.

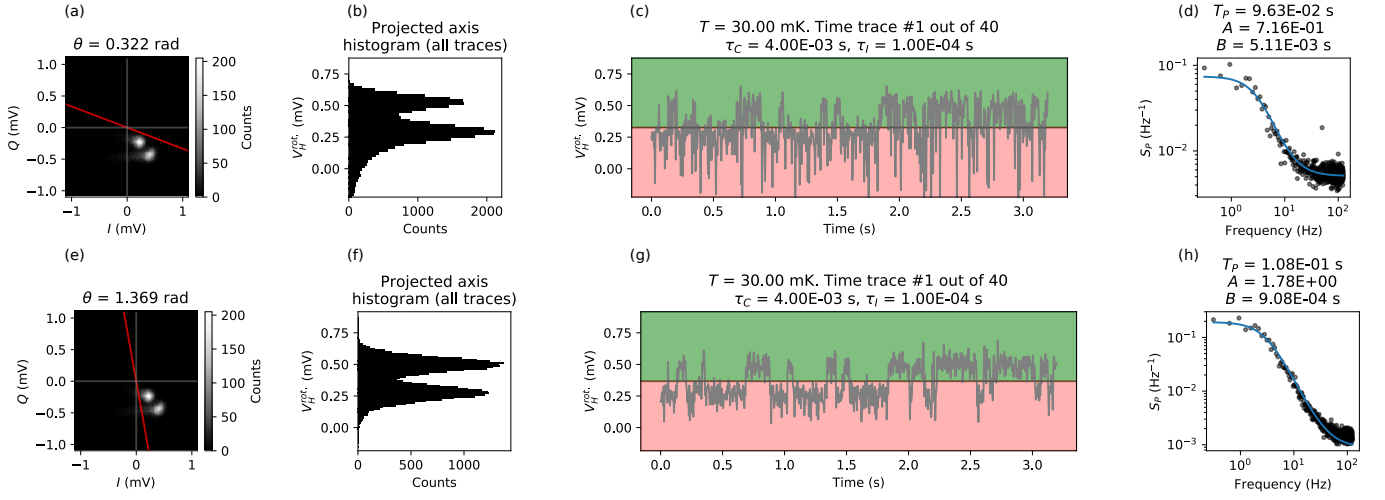


FIG. S1. Plots used to select phase-quadrature-plane rotation angle θ . Two different θ for the data set in Fig. 1(c-d). In (a-d) $\theta = 0.322$ rad. (a) Two-dimensional histogram with the red line indicating θ . The extension of each population are interpreted to result from residual excited state population. (b) One-dimensional histogram of the data rotated by θ . (c) One of the N_T traces; here $N_T = 40$. (d) Average PSD of all N_T data sets. (e-h) as (a-d) but with $\theta = 1.369$ rad, which was selected for obtaining the T_P value in the main text from this data.

Parity data post-selection

Here we describe how the two-tone spectroscopy data in Fig. 2(b) were post-selected into separate parity branches. As shown in Fig. S2, the rows are divided into segments AB, BC, etc. Rows are post-selected into parities based on whether the value at a specific point is higher or lower than the mean of that row. The columns picked for the sorting are shown as vertical lines in Fig. S2. This particular procedure relies on a feature unique to one of the parities existing in every row.

Destructive Little-Parks effect

Similar to Ref. 13, the NW for which we measure T_P here exhibits a destructive Little-Parks effect. This can be directly seen in the two-tone spectroscopy measurement of qubit frequency f_{01} as a function of magnetic field, shown

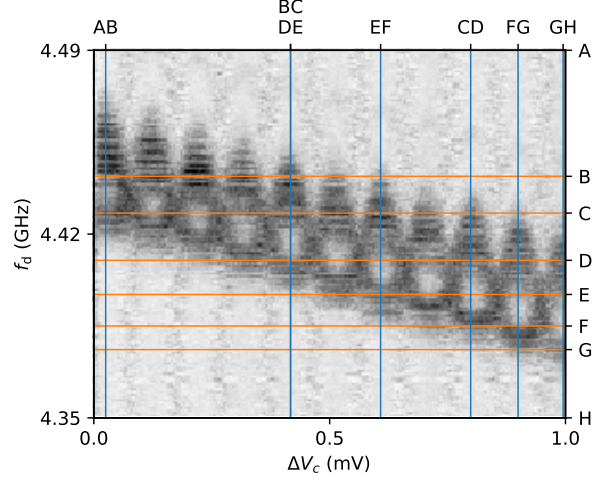


FIG. S2. Criterion points used in the parity post-selection for spectroscopy. For a given interval of f_d , data are post-selected conditioned on the value at a chosen ΔV_c (e.g. at AB for $A > f_d > B$) exceeding the mean of that trace of V_H as a function of V_c .

in Fig. S3. Following Ref. 13, the pair-breaking term α is given minimizing the function [12, 31, 32],

$$\alpha(B) = \frac{4\xi^2 k_B T_{C0}}{\pi R^2} \left[\left(n - \frac{\Phi}{\Phi_0} \right)^2 + \frac{t^2}{4R^2} \left(\frac{\Phi^2}{\Phi_0^2} + \frac{n^2}{3} \right) \right] \quad (3)$$

in the winding number n at each B , where ξ is the superconducting coherence length at zero field, T_{C0} is the critical temperature at zero field, Φ is the applied magnetic flux, R is the radius of the superconducting shell, and t is the shell thickness. The pairing energy Δ is then found by solving the implicit equation [33]

$$\log \frac{\Delta_0}{\Delta} = \begin{cases} \frac{\pi\alpha}{4\Delta}, & \text{if } \alpha < \Delta, \\ \log \left(\frac{\alpha + \sqrt{\alpha^2 - \Delta^2}}{\Delta} \right) - \frac{\sqrt{\alpha^2 - \Delta^2}}{2\alpha} + \frac{\alpha}{2\Delta} \arcsin \frac{\Delta}{\alpha}, & \text{if } \Delta > \alpha. \end{cases} \quad (4)$$

We assume that Δ enters the transmon Hamiltonian as $E_J = (\Delta/4) \sum \eta$ where η are the transmissions of the JJ channels. In terms of Δ , the spectral gap ω is given by [33]

$$\omega = \left(\Delta^{2/3} - \alpha^{2/3} \right)^{3/2}. \quad (5)$$

We assume that ω enters into Eq. (2).

Transmission electron micrographs of nanowires

Transmission electron micrographs of NWs from the same growth batch as the NW used in the device described in the main text, are shown in Fig. S4. Differences between NWs in micrographs and the one used for the device might exist, due to aging, position on wafer, and individual wire-to-wire variations.

Experimental setup

A diagram of the experimental setup is shown in Fig. S5. The sample is mounted on a printed circuit board in an In-sealed CuBe box, with added Eccosorb foam.

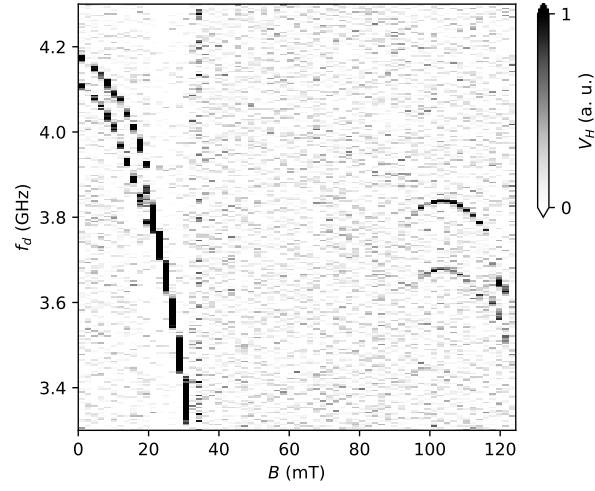


FIG. S3. Destructive Little-Parks effect observed by measuring the qubit frequency f_{01} , resulting in a lobe structure as a function of magnetic field B .

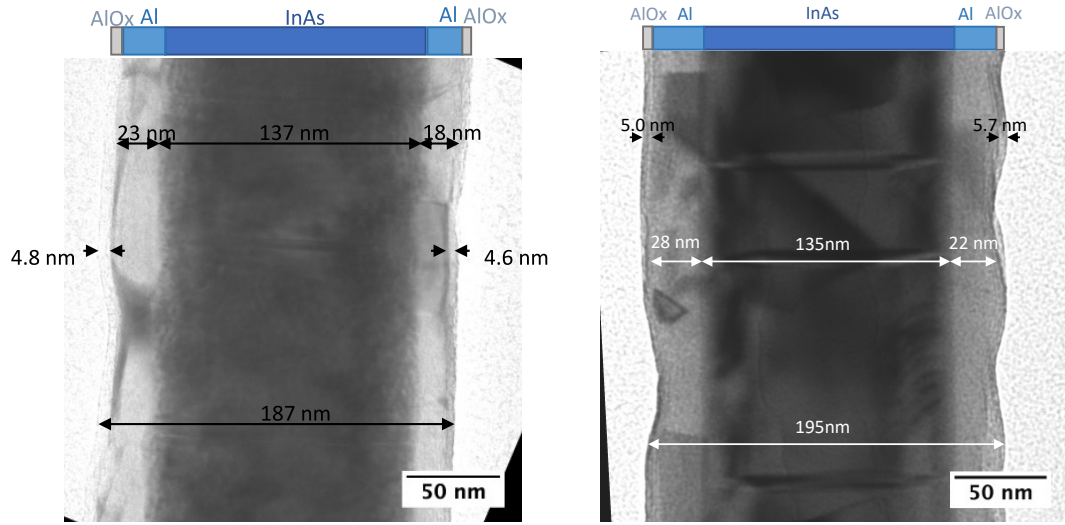


FIG. S4. Transmission electron micrographs of two NWs from the same growth batch as the NW discussed in the main text, with physical dimensions indicated.

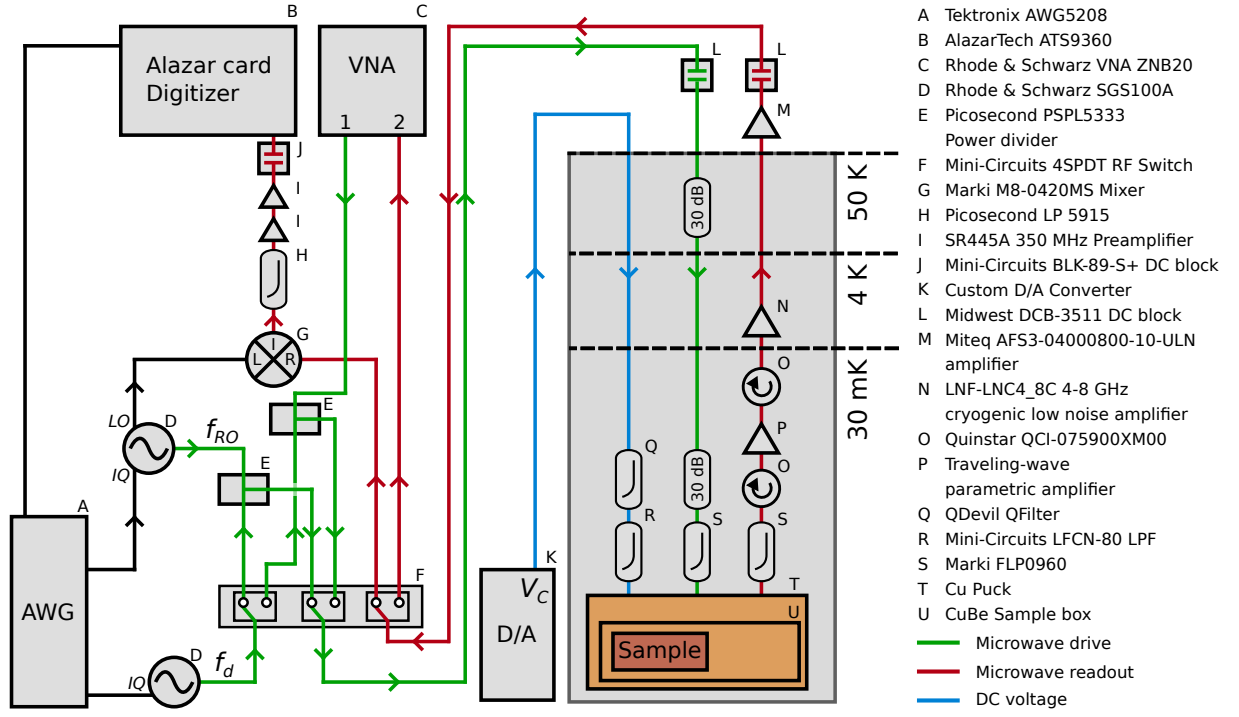


FIG. S5. Experimental setup.